HHS Public Access

Author manuscript

Dev Biol. Author manuscript; available in PMC 2017 March 01.

Published in final edited form as:

Dev Biol. 2016 March 1; 411(1): 15–24. doi:10.1016/j.ydbio.2016.01.015.

The SWI/SNF BAF-A complex is essential for neural crest development

Ronald L. Chandler[1] and **Terry Magnuson**[1,+]

[1]Department of Genetics, University of North Carolina at Chapel Hill

Abstract

Growing evidence indicates that chromatin remodeler mutations underlie the pathogenesis of human neurocristopathies or disorders that affect neural crest cells (NCCs). However, causal relationships among chromatin remodeler subunit mutations and NCC defects remain poorly understood. Here we show that homozygous loss of ARID1A-containing, SWI/SNF chromatin remodeling complexes (BAF-A) in NCCs results in embryonic lethality in mice, with mutant embryos succumbing to heart defects. Strikingly, monoallelic loss of ARID1A in NCCs led to craniofacial defects in adult mice, including shortened snouts and low set ears, and these defects were more pronounced following homozygous loss of ARID1A, with the ventral cranial bones being greatly reduced in size. Early NCC specification and expression of the BRG1 NCC target gene, PLEXINA2, occurred normally in the absence of ARID1A. Nonetheless, mutant embryos displayed incomplete conotruncal septation of the cardiac outflow tract and defects in the posterior pharyngeal arteries, culminating in persistent truncus arteriosus and agenesis of the ductus arteriosus. Consistent with this, migrating cardiac NCCs underwent apoptosis within the circumpharyngeal ridge. Our data support the notion that multiple, distinct chromatin remodeling complexes govern genetically separable events in NCC development and highlight a potential pathogenic role for NCCs in the human BAF complex disorder, Coffin-Siris Syndrome.

Keywords

ARID1A; BAF-A; SWI/SNF; Neural Crest; Coffin-Siris Syndrome

Introduction

The neural crest is a multipotent cell population that arises from the dorsal neural tube. Following induction, neural crest cells (NCCs) delaminate and migrate throughout the embryo where they further differentiate into diverse cell types, including bone and cartilage cells, peripheral neurons and glia, melanocytes, and smooth muscle cells (Keyte and Hutson, 2012; Kirby and Hutson, 2010). Cranial NCCs originating from rostral locations contribute to the frontonasal skeleton and membranous bones of the face, whereas those originating

[+]denotes Corresponding Author. Address inquiries to trm4@med.unc.edu.

from more caudal positions, between the mid-otic placode and posterior border of somite four, give rise to the cardiac neural crest and populate the pharyngeal arch arteries (PAA) and heart outflow tract (OFT) (Brown and Baldwin, 2006; Keyte and Hutson, 2012; Lin et al., 2012). In addition to their contributions to smooth muscle and connective tissue, cardiac NCC interactions with other cell types within the pharyngeal arch apparatus pattern the great arteries of the heart (Keyte and Hutson, 2012; Kirby and Hutson, 2010). A full understanding of the underlying molecular mechanisms involved in NCC biology is key to advancing our understanding of human cardio-craniofacial disorders or other putative neurocristopathies, including 22q-deletion/DiGeorge/velocardiofacial, CHARGE and Coffin-Siris syndromes.

Coffin-Siris syndrome (CSS) (MIM 135900) is congenital associated with intellectual disability or developmental delay, hypoplastic fifth fingernails, and patterning defects in the head (broad nasal bridge, low set ears, cleft palate, choanal atresia, hearing loss) and heart (ventricular septal defects or VSDs, malposition of great arteries, and patent ductus arteriosus) (Kosho et al., 2014; Kosho et al., 2013; Schrier et al., 2012). The most severe cases of CSS result in intrauterine or early childhood death with associated cardiac defects (Coulibaly et al., 2010; Kosho et al., 2014; Kosho et al., 2013; Nemani et al., 2014; Santen et al., 2013). Remarkably, 87% of individuals with CSS have *de novo* autosomal dominant mutations in one of six SWI/SNF chromatin-remodeling complex subunits, including ARID1A, ARID1B, BRG1, BRM, SNF5/INI1, or BAF57 (Kosho et al., 2014; Kosho et al., 2013; Santen et al., 2012; Tsurusaki et al., 2012). All of the known SWI/SNF mutations in CSS are restricted to subunits found within ARID1A or -1B-containing BAF (BRG1/BRM-associated factor) sub-complexes, but not ARID2-containing PBAF (Polybromo- BRG1-associated factor) sub-complexes (Kosho et al., 2014). In addition to those mutations found in CSS, ARID1A and -1B are mutated in a subset of childhood neuroblastomas, which originate from NCC derivatives (Sausen et al., 2013). These findings are the first to demonstrate that mutations in genes encoding diverse BAF subunits result in similar human disease phenotypes, and that BAF complex mutations underlie the etiology of a human congenital disease.

Recent functional studies have highlighted a role for the SWI2/SNF2-family of chromatin remodelers in NCCs. Cooperativity between CHD (chromodomain helicase DNA-binding domain) and PBAF remodelers are required to activate early neural crest transcriptional programs, and this interaction is implicated in the pathogenesis of CHARGE syndrome (Bajpai et al., 2010). Disruption of the SWI/SNF catalytic subunit, BRG1, in mouse NCCs results in cerebral hemorrhaging, severe PAA defects, and shortened OFTs, culminating in death by embryonic day (E) 12.5 (Li et al., 2013). In addition, BRG1 interactions with CHD7 at the PLEXINA2 promoter, perhaps via PBAF, are required to activate PLEXINA2 expression and promote early cardiac NCC fates (Li et al., 2013). However, it is unclear if BRG1 is functioning through BAF- or PBAF-related mechanisms, or both, in NCCs and whether BAF complex mutations, as observed in CSS, recapitulates CSS-like phenotypes in mice. In this study, we investigate the cell autonomous role of ARID1A-containing BAF complexes (herein called BAF-A) within the developing neural crest using conditional deletion strategies in mice.

Material and Methods

Mouse husbandry and genotyping

All mice were maintained on an outbred (random) genetic background and identified by PCR using published methods (Chai et al., 2000; Chandler et al., 2015; Danielian et al., 1998; Jiang et al., 2000). All mice were maintained at the University of North Carolina at Chapel Hill, Animal Facility using standard techniques in accordance with protocols approved by the University of North Carolina at Chapel Hill Institutional Animal Care and Use Committee.

In situ hybridization, immunostaining, β-GALACTOSIDASE, TUNEL assays and whole mount cell death staining and histology

In situ hybridization was performed as described previously (Acloque et al., 2008; Jacques-Fricke et al., 2012; Nieto et al., 1996; Wilkinson and Nieto, 1993) with antisense probes to PLEXINA2 (Brown et al., 2001) (Addgene plasmid 16423), KROX20 (Wilkinson et al., 1989), SOX10 (Southard-Smith et al., 1998)(Addgene plasmid 24752), DLX5 (Zerucha et al., 2000) (Addgene plasmid 15538), SM22α-(Li et al., 1996), HOXD3 (Minoux et al., 2009), MSX1 (Ishii et al., 2005), and MSX2 (Ishii et al., 2003). The ARID1A probe was generated by PCR sub-cloning a mouse ARID1A cDNA fragment into pGEM T-Easy using the following gene specific primers: (F) CCACCAGGCTACCCAAATATGAATCAAGGG; (R) CCTCATGCTGCCATAAGGATCCTTATTTGGCTC. For direct fluorescent immunostaining, the embryos were fixed for 20 min. in cold, fresh 10% neutral buffered formalin (Sigma), washed in cold 1× phosphate buffered saline (PBS), and then cryo-protected through a graded sucrose series at 4°C. Specimens were then embedded on dry ice. Samples were sectioned at 10 μm and collected on Superfrost-Plus slides (Fisher). Frozen sections were briefly thawed on a 42°C slide warmer, equilibrated in 1× PBS, and then incubated for 45 min. in 100 mM glycine; 1× PBS [pH 7.3]. Block and antibody diluent consisted of 1× PBS–0.05% Tween-20 supplemented with 5% normal serum (Jackson Immuno.), 1% (w/v) BSA, and 0.1% (w/v) cold-water fish gelatin (Sigma). Slides were incubated in a 1:50 dilution of anti-ARID1A (sc-32761, Santa Cruz Biotechnology), 1:200 dilution of anti-P75 (G3231, Promega), or 1:200 dilution of anti-β-GALACTOSIDASE (ab9361, Abcam) antibodies followed by detection with a species-specific, fluorescently conjugated secondary antibody (Jackson Immuno.). Slides were mounted and coverslipped in 4′, 6′–diamidino-2-phenylindole (DAPI)–containing, Prolong-Gold medium (Invitrogen). Whole mount immunostaining for PECAM1 (CD-31) was performed as described using a monoclonal rat anti-mouse CD31 antibody (BD Biosciences; MEC13.3) (Chandler et al., 2013; Griffin et al., 2008). Whole mount β-GALACTOSIDASE staining was performed as previously described (Chandler et al., 2007). Whole mount cell death staining was performed as previously described using Lysotracker Red (Molecular Probes) (Zucker et al., 1999). Lysotracker Red-stained embryos were fixed for 2 hours in 4% paraformaldehyde–1× PBS, washed in PBT (1× PBS supplemented with 0.1% (v/v) Tween-20), and then transferred to 100% methanol through a graded methanol-PBT series. The embryos were then stored overnight at −20°C to facilitate permeabilization. Rehydrated embryos were equilibrated in 1× PBSTX (1× PBS supplemented with 0.3% (v/v) Triton X-100 and then blocked for 2 days at 4°C in blocking buffer (1× PBS supplemented with 0.3% (v/v) Triton

X-100, 5% (v/v) normal serum and 50% (v/v) Pierce SuperBlock-PBS reagent). The embryos were incubated with a 1:100 dilution of anti-SOX10 antibody (sc-17342, Santa Cruz Biotechnology) overnight at 4°C in blocking buffer, and washed 5–7 times in 1× PBSTX for 5–7 consecutive days at 4°C, followed by detection with a species-specific, fluorescently conjugated secondary antibody (Jackson Immuno.). TUNEL assays were performed using the DeadEnd Fluorometric TUNEL System (Promega) according to the manufacturer's instructions. Routine histological sections and Hematoxylin and Eosin (H&E) staining were performed by University of North Carolina, Lineberger Cancer Center, Animal Histopathology Core.

India ink injections

The cardiac ventricles of live embryos were injected with an undiluted black India ink solution (American Master Tech) using a pulled glass capillary needle. The embryos were then fixed in fresh 4% paraformaldehyde-1× PBS, imaged and stored in 70% ethanol.

Imaging and morphometric analysis

Histological sections were analyzed and photographed on an Olympus BX51 microscope using bright-field optics and a DP series digital camera (Olympus). Whole mount embryo specimens were imaged on a Leica MZ FLIII stereomicroscope using a DS Ri1 digital camera (Nikon). Measurements and morphometric analysis of whole mount skeletons were performed using Elements software (Nikon). Fluorescent microscopy and image acquisition were performed using a Leica DM LB microscope and a Retiga-2000R digital camera (Q-Imaging).

Results

Monoallelic loss of ARID1A in NCCs results in mild craniofacial defects

To examine BAF-A function in NCCs, we conditionally deleted ARID1A by crossing our *Arid1a*^{fl} allele (Chandler et al., 2015) with *Wnt1CRE* transgenic mice (Chai et al., 2000; Danielian et al., 1998; Jiang et al., 2000). Monoallelic loss of ARID1A in NCCs led to shortened snouts, low set ears, and sunken eyes (Fig. 1A, K). Head skeleton morphometric measurements revealed smaller squamosal bones and shortened pre-maxilla bones (Fig. 1B–E, K). In addition, the anterior palantine length of *Arid1a*$^{fl/+}$*; Wnt1Cre* mice was reduced (Fig. 1H–I, K). The body mass of *Arid1a*$^{fl/+}$*; Wnt1Cre* was less than littermate controls, but both heterozygous and wild-type mice had similar intercanthal distance and molar width measurements, suggesting that the craniofacial defects we observed are not due to proportional body size differences (Fig. 1F–K).

ARID1A inactivation in NCCs results in craniofacial defects

ARID1A is a ubiquitously expressed subunit in the BAF complex (Dallas et al., 2000); (Inoue et al., 2002); (Nie et al., 2000); (Nie et al., 2003). We further observed widespread ARID1A expression by whole mount in situ hybridization on E9.5 and E10.5 mouse embryos, including NCC-derived tissues of the head and pharyngeal arches (Fig. 2A, B). To further examine BAF-A function and determine the phenotypic consequences of complete ARID1A loss in NCCs, we generated *Arid1a*$^{fl/fl}$*; Wnt1Cre* mice. To confirm ARID1A

deletion in NCCs, we immunostained E10.5 *Arid1a*$^{fl/fl}$*; Gt(ROSA)26*^{tm1Sor}*; Wnt1Cre* embryo sections of the dorsal neural tube or head mesenchyme using an anti-ARID1A antibody (Fig. 2C–F). The *Gt(ROSA)26*^{tm1Sor} allele (Soriano, 1999) was used to monitor Wnt1CRE activity in premigratory and migratory NCCs and *lacZ* expression was detected using an anti-β-GALACTOSIDASE (β-GAL) antibody (Fig. 2C,E). An anti-P75 pan-neurotrophin receptor antibody further identified NCCs within the head mesenchyme (Fig. 2D,F). In control embryos, ARID1A is expressed throughout non-NCC and NCC-derived cell populations in the neural tube and head (Fig. 2C,D). We found that ARID1A expression in β-GAL- and P75-positive NCCs was undetectable in *Arid1a*$^{fl/fl}$*; Gt(ROSA)26*^{tm1Sor} *Wnt1Cre* embryos (Fig. 2E,F). These data demonstrate that ARID1A is expressed in NCCs and that *Wnt1CRE* effectively removes ARID1A function from this cell population.

Arid1a$^{fl/fl}$*; Wnt1Cre* embryos were recovered at normal Mendelian ratios until E15.0 (Table 1). Late gestation embryos were grossly abnormal with pronounced head defects, including a small head size, depressed cranial vaults, low set eyes and ears, and shortened snouts (Fig. 3B). Head skeleton preparations revealed normally patterned, yet ventrolaterally positioned, dorsal cranial bones, including the frontal and parietal bones (Fig. 3D). However, most of the bones that form the ventral cranial skeleton were greatly reduced in size (Fig. 3D). This lack of ventral cranial vault support likely contributed to the ventrolateral movement of the frontal and parietal bones and eye sockets or ear canals, leading to “droopy” or low-set facial features. In general, the same ventral cranial bones affected in homozygous *Arid1a*$^{fl/fl}$*; Wnt1Cre* embryos were also affected in heterozygous *Arid1a*$^{fl/+}$*; Wnt1Cre* mice, albeit with striking differences in phenotypic severity (Fig. 3E).

MSX1 and MSX2 are expressed in migratory NCCs and NCC-derived mesenchyme of the pharyngeal arches, and loss of MSX1 and MSX2 in NCCs leads to craniofacial defects due to impaired survival of pharyngeal arch (PA) 1 NCC derivatives. (Ishii et al., 2005). PA1 NCC derivatives originate from posterior mesencephalic and rhombencephalic NCCs and give rise to components of the ventral facial skeleton, mandible and otic capsule (Santagati and Rijli, 2003). In *Arid1a*$^{fl/fl}$*; Wnt1Cre* embryos, MSX1 expression is reduced in a small ventral portion of the mandibular region of PA1 corresponding the rostral end of the pharyngeal pouch, whereas MSX2 expression in this area is dramatically reduced or absent in mutant embryos (Fig. 3G,I). We also observed increased apoptosis in the ventral half of mandibular region of PA1 by TUNEL labeling, suggesting that loss of PA1 NCC derivatives contributes to agenesis of mandible and ventral bones of late gestation *Arid1a*$^{fl/fl}$*; Wnt1Cre* embryos (Fig. 3K). These data suggest that BAF-A complexes are required for the survival of NCCs that give rise to ventral cranial skeleton and jaw.

Loss of ARID1A-containing BAF-A complexes leads to defects in early migrating cardiac NCCs

PLEXINA2 labels premigratory NCCs in the dorsal neural tube and has previously been shown to be a direct target SWI/SNF activity in NCCs, based upon the phenotypes reported Li *et al.* in *Brg1*$^{fl/fl}$*; Wnt1Cre* embryos (Brown et al., 2001; Li et al., 2013). ARID1A loss did not lead to changes in PLEXINA2 expression within this region and uniform PLEXINA2 expression was observed in an “unbroken” stripe pattern along the entire length

of the dorsal neural tube in both control and mutant wholemount embryos (Fig. 4A,D, see cross-sectional images inset). Thus, early specification of premigratory NCCs likely proceeds normally in *Arid1a*$^{fl/fl}$*; Wnt1Cre* embryos.

KROX20 is expressed in rhombomeres 3 and 5 of the neural tube and in rhombomere 5/6-derived, post-otic migratory NCCs (Ghislain et al., 2003; Schneider-Maunoury et al., 1993). Post-otic NCCs are thought to populate the third branchial arch and give rise to a subset of cardiac NCC derivatives in the OFT (Ghislain et al., 2003; Schneider-Maunoury et al., 1993). In both control and *Arid1a*$^{fl/fl}$*; Wnt1Cre* embryos, we observed normal patterns of KROX20 expression in rhombomeres 3 and 5 (Fig. 4B,E). However, KROX20 expression was severely reduced in migrating post-otic NCC streams of *Arid1a*$^{fl/fl}$*; Wnt1Cre* (Fig. 4E, arrowheads).

To further examine migratory NCC populations in *Arid1a*$^{fl/fl}$*; Wnt1Cre* embryos, we utilized the multipotent, migratory neural crest marker, SOX10 (Deal et al., 2006; Southard-Smith et al., 1998). The overall pattern of SOX10 expression in migratory neural crest streams and sensory ganglia along anterior-posterior axis was similar in both E9.5 *Arid1a*$^{fl/fl}$*; Wnt1Cre* and control embryos (Fig. 4C,F). In contrast, SOX10 expression in post-otic, cardiac neural crest streams originating from rhombomeres 5–8 and migrating through the circumpharyngeal ridge was reduced (Fig. 4F, arrowheads). Likewise, fewer β-GAL-positive cells were observed in post-otic streams and in the circumpharyngeal ridge of E9.5 *Arid1a*$^{fl/fl}$*; Gt(ROSA)26*^{tm1Sor}*;Wnt1Cre* embryos, but the overall pattern of β-GAL expression in the remaining NCC streams of the head and trunk remained largely unchanged when compared to controls, similar to the SOX10 expression patterns (Fig. 4G,H). Together, these data suggest that loss of BAF-A complexes leads to defects in cardiac NCCs.

BAF-A complexes are essential for NCC colonization and patterning of the cardiac outflow tract

Proper cardiac OFT septation and great vessel patterning is essential for mammalian development and dependent on cardiac NCCs (Copp, 1995; Lin et al., 2012). To determine the cause of lethality in *Arid1a*$^{fl/fl}$*; Wnt1Cre* embryos, we focused on cardiac NCCs, given the NCC cardiac lineage alterations we observed in E9.5 embryos. We used the CRE inducible *Gt(ROSA)26*^{tm1Sor} allele to label cardiac NCC derivatives at mid-gestational timepoints when cardiac NCC colonization and early outflow tract septation are occurring. The depth of cardiac OFT penetration by ARID1A mutant NCCs was reduced and elongation of the outflow tract apparatus was truncated in E10.5 *Arid1a*$^{fl/fl}$*; Gt(ROSA)26*^{tm1Sor}*; Wnt1Cre* embryos, resulting shortened outflow tracts (Fig. 5F,I,K). We further validated these findings by wholemout *in situ* hybridization using SM22α (TRANSGELIN) and PLEXINA2 antisense probes, which labels NCC-derived vascular smooth muscle and NCCs of the OFT, respectively (Fig. 5B,G). Aorticopulmonary septation of the OFT of wild-type embryos was evident as early at E10.5 (Fig. 5A,D,E, arrowheads). By E11.5, a clear “spiraling” of the conotruncal septum and separation of future pulmonary artery and aorta was observed in the control embryos (Fig. 5E). In contrast, the outflow tracts of *Arid1a*$^{fl/fl}$*; Gt(ROSA)26*^{tm1Sor}*; Wnt1Cre* embryos showed no evidence of conotruncal septation at these stages (Fig. 5F–J). Together, these data demonstrate that loss

of an ARID1A-containing BAF complex in NCCs results incomplete cardiac NCC colonization of the outflow tract and septation of the arterial trunk.

BAF-A loss leads to defects in the circumpharyngeal cardiac NCC

Cardiac NCCs migrating along dorsolateral paths traverse the circumpharyngeal ridge and pattern the posterior PAAs (Kirby and Hutson, 2010; Kuratani and Kirby, 1992). To examine *Arid1a*$^{fl/fl}$*; Wnt1Cre* embryos for PAA defects, we used a combination of India ink angiography and vessel endothelium or PAA marker gene expression. All of the E10.5 *Arid1a*$^{fl/fl}$*; Wnt1Cre* embryos examined by India ink angiography displayed thin- or non-patent left and right PAA6 defects (Fig. 6I and Table 2). A subset of mutant embryos had thin- or, to a lesser extent, non-patent PAA4 defects and larger diameter PAA3 vessels (Fig. 6I, and Table 2). We further validated our findings by *in situ* hybridization using a DLX5 antisense probe, which labels the NCC-derived pharyngeal arch mesenchyme (Fig. 6C,K). Loss of ARID1A led to loss of DLX5 expression in pharyngeal arch 6, further supporting a role for BAF-A complexes in posterior cardiac NCC derivatives (Fig. 6K).

To explore the fate of posterior cardiac NCC derivatives further, we focused on NCCs migrating through the circumpharyngeal ridge. At E10.5, cardiac NCCs are migrating in post-otic and circumpharyngeal streams, as evidence by SOX10 expression patterns (Fig. 6D,F). *Arid1a*$^{fl/fl}$*; Wnt1Cre* embryos displayed reduced SOX10 expression in the circumpharyngeal stream and, to a lesser extent, in the more anterior post-otic stream at E10.5, similar to our findings at earlier timepoints (Fig. 6L,N). Concomitantly, apoptotic cells were detected in circumpharyngeal ridge, as shown by whole mount lysotracker red staining and TUNEL labeling (Fig. 5M,N,R). Expression of HOXD3, a marker of circumpharyngeal ridge NCCs and mesenchyme, was also reduced in E10.5 mutant embryos (Fig. 6O) (Minoux et al., 2009). In addition, fewer β-GAL-positive, mutant NCC cells were observed in post-otic and circumpharyngeal streams of E10.5 *Arid1a*$^{fl/fl}$*; Gt(ROSA)26*^{tm1Sor}*; Wnt1Cre* embryos, similar to earlier timepoints (Fig. 6P). These data suggest that improper colonization of posterior cardiac NCCs leads to increased apoptosis in the circumpharyngeal ridge, resulting in posterior PAA defects and incomplete PAA6 formation in mutant embryos.

Posterior PAA development is required for the formation of the ductus arteriosus, thus proper embryonic blood flow (Copp, 1995). Consistent with this, E12.5 *Arid1a*$^{fl/fl}$*; Wnt1Cre* embryos failed to form a PAA6-derived ductus arteriosus, as shown by wholemount SM22α-labeling of heart vessels (Fig. 6W,X). We also observed patterning defects in the remaining great vessels of mutant embryos at this stage (Fig. 6W,X). Together, the lack of outflow tract septation and incomplete formation of ductus arteriosus culminated in persistent truncus arteriosus and embryonic death in *Arid1a*$^{fl/fl}$*; Wnt1Cre* embryos (Fig. 6Y). We also observed incomplete formation of ventricular septum and misaligned or abnormally patterned pulmonary and aortic valves, suggesting that ventricular septal defects (VSDs) are present in late-gestation ARID1A NCC mutants (Fig. 6Z). These findings support an essential role for ARID1A-containing, BAF complexes in cardiac neural crest development.

Conclusion

We have demonstrated that ARID1A-containing, BAF complexes are essential for NCC development and that ARID1A NCC mutants die *in utero* because of defects in migrating post-otic and circumpharyngeal cardiac NCC populations (Fig. 6). Our data support the notion that multiple, distinct SWI/SNF chromatin remodelers play essential roles at distinct stages of NCC development and strongly suggest that BAF complex mutations in NCCs contribute to the pathophysiology of putative human cardio-craniofacial syndromes. We propose that a subset of the constellation of congenital abnormalities observed in CSS patients with ARID1A or BAF complex subunit mutations arise from embryonic defects in the NCC lineage.

Discussion

Our findings suggest that multiple, biochemically distinct SWI/SNF complexes regulate several aspects of NCC development. For example, Li et al. (Li et al., 2013) previously reported that BRG1 NCC conditional mutants (via *Wnt1CRE*) are not recovered past E12.5 and that mutant embryos succumb to death due to hemorrhaging. In addition, expression of the BRG1 target gene, PLEXINA2, was lost in *Brg1$^{fl/fl}$; Wnt1Cre* mutant embryos (Li et al., 2013). On the other hand, 100% of *Arid1a$^{fl/fl}$; Wnt1Cre* embryos are recovered up until E14.5, with death occurring at later stages of gestation. The majority of *Arid1a$^{fl/fl}$; Wnt1Cre* embryos also manifested prominent cranial bone defects at these later timepoints. Moreover, early expression of PLEXINA2 in the dorsal neural tube was unaffected following loss of ARID1A in NCCs via *Wnt1CRE*. In spite of these differences, loss of BRG1 and ARID1A in NCCs led to OFT and PAA patterning defects, albeit with slight differences in phenotypic severity and PAA involvement. Within the PAA apparatus, loss of BRG1 in NCCs was reported to lead defects in the anteriorly positioned PAA3 and PAA4 arteries (Li et al., 2013), whereas ARID1A loss contributed to defects in the more posteriorly positioned PAA6 artery, which is consistent with the late gestation heart patterning defects we observed. Thus, clear phenotypic differences arise following NCC-specific loss of BAF complex subunits.

The involvement of the SWI2/SNF2-family of chromatin remodeling complexes at various stages of the NCC development and the identification chromatin remodeling subunit mutations in human neurocristopathies highlight the diverse, yet cell autonomous, roles of chromatin remodelers within the NCC lineage. Cooperation between CHARGE Syndrome candidate gene, CHD7, and PBAF in human neural crest-like stem cells and *Xenopus laevis* is required to activate the early NCC-specific transcriptional programs and cell migration (Bajpai et al., 2010). In addition, BRG1 interactions with CHD7 were reported to be important for PLEXINA2 activation (Li et al., 2013). Currently, it is unclear if PBAF inactivation in mouse NCCs will recapitulate the phenotypes observed in BRG1 NCC mutants or if PBAF interactions with CHD7 promote PLEXINA2 activation or the activation of additional NCC-specific programs in both premigratory and migratory NCCs. Moreover, the expression certain chromatin remolding subunits might be higher or enriched in different NCC populations, despite a near ubiquitous pattern of expression. For example, ARID1A-containing, BAF complexes may lead to severe defects in cardiac NCC

populations because this is the predominant form of the SWI/SNF complex in this cell population. Nonetheless, our data suggest that additional BRG1-containing, SWI/SNF complexes are functioning at earlier stages of NCC development or acting redundantly to compensate for loss of ARID1A in NCCs, as would be the case in *Arid1a*$^{fl/fl}$*; Wnt1Cre* mutant NCCs, which are predicted to have intact SWI/SNF complexes with alternative ARID subunits. Additional genetic experiments using ARID2 and ARID1B conditional alleles will help to address these possibilities and resolve the phenotypic differences observed in ARID1A and BRG1 NCC mutants.

CSS is a rare, orphan human congenital disease that affects several body systems, but it is not typically classified as a neurocristopathy. CSS patients with heterozygous loss-of-function (haploinsufficient) ARID1A mutations manifest the most severe defects, and most ARID1A mutations are predicted to be mosaic in somatic tissues (Coulibaly et al., 2010; Kosho et al., 2014; Kosho et al., 2013; Nemani et al., 2014; Santen et al., 2013). Interestingly, one CSS patient with ARID1A mutations was diagnosed with phenotypic features similar to Hirschsprung's disease, a known neurocristopathy (Santen et al., 2013). We failed to detect heart defects in heterozygous *Arid1a*$^{fl/+}$*; Wnt1Cre* mice, despite the observation that the most frequent complications observed in CSS patients with BAF complex mutations are palatal abnormalities and heart defects (Coulibaly et al., 2010; Kosho et al., 2014; Kosho et al., 2013; Nemani et al., 2014; Santen et al., 2013). In spite of these mouse-human differences, some of the shared phenotypic features observed in CSS patients are found among other human neurocristopathies, such as CHARGE syndrome, or conferred through the phenotypes observed in ARID1A NCC mutant embryos. First, heterozygous *Arid1a*$^{fl/+}$*; Wnt1Cre* mice displayed craniofacial defects, including low set ears. Second, the spectrum of NCC heart defects observed in *Arid1a*$^{fl/fl}$*; Wnt1Cre* embryos are consistent with the heart defects observed in human patients, albeit with differing ARID1A gene dosage sensitivities and phenotypic severity (Kosho et al., 2014). Based on these findings, we suggest that CSS represents a collective of anomalies with embryonic origins in both NCCs and other cell types or tissues, similar to CHARGE syndrome. It remains possible that *de novo* human ARID1A mutations also affect NCC development in a non-cell-autonomous manner, perhaps through neural tube or pharyngeal arch defects. An improved understanding of BAF complex subunit mutations, how these mutations influence BAF complex function, and the further identification of tissues or cell types that are sensitive to BAF complex loss will add clarity to CSS genotype-phenotype relationships.

Acknowledgments

We thank members of the Magnuson Lab for their helpful discussions. We also thank Dr. Anna Spagnoli for generously sharing imaging equipment, Drs. Mamoru Ishii and Robert Maxson for providing the Krox20 and Hoxd3 probes courtesy of Dr. Henry Sucov and MSX1 and MSX2 probes courtesy of Dr. Yi-Hsin Liu, Dr. Tsutomu Kume for the SM22α-probe, Drs. Julaine Roffers-Agarwal and Laura Gammill for their mouse whole mount *in situ* hybridization protocol, and Drs. Nathan Mundell and Patricia Labosky for their guidance and advice.

A Postdoctoral Fellowship (PF-09-116-01-CCG) from the American Cancer Society and an Ann Schreiber Mentored Investigator Award (258831) from the Ovarian Cancer Research Fund to R.L.C. and NIH grants to T.M. (HD03665) supported this work.

Bibliography

Acloque H, Wilkinson DG, Nieto MA. In situ hybridization analysis of chick embryos in whole-mount and tissue sections. Methods in cell biology. 2008; 87:169–185. [PubMed: 18485297]

Bajpai R, Chen DA, Rada-Iglesias A, Zhang J, Xiong Y, Helms J, Chang CP, Zhao Y, Swigut T, Wysocka J. CHD7 cooperates with PBAF to control multipotent neural crest formation. Nature. 2010; 463:958–962. [PubMed: 20130577]

Brown CB, Baldwin HS. Neural crest contribution to the cardiovascular system. Advances in experimental medicine and biology. 2006; 589:134–154. [PubMed: 17076279]

Brown CB, Feiner L, Lu MM, Li J, Ma X, Webber AL, Jia L, Raper JA, Epstein JA. PlexinA2 and semaphorin signaling during cardiac neural crest development. Development. 2001; 128:3071–3080. [PubMed: 11688557]

Chai Y, Jiang X, Ito Y, Bringas P Jr, Han J, Rowitch DH, Soriano P, McMahon AP, Sucov HM. Fate of the mammalian cranial neural crest during tooth and mandibular morphogenesis. Development. 2000; 127:1671–1679. [PubMed: 10725243]

Chandler RL, Brennan J, Schisler JC, Serber D, Patterson C, Magnuson T. ARID1a-DNA interactions are required for promoter occupancy by SWI/SNF. Molecular and cellular biology. 2013; 33:265–280. [PubMed: 23129809]

Chandler RL, Chandler KJ, McFarland KA, Mortlock DP. Bmp2 transcription in osteoblast progenitors is regulated by a distant 3′ enhancer located 156.3 kilobases from the promoter. Molecular and cellular biology. 2007; 27:2934–2951. [PubMed: 17283059]

Chandler RL, Damrauer JS, Raab JR, Schisler JC, Wilkerson MD, Didion JP, Starmer J, Serber D, Yee D, Xiong J, Darr DB, Pardo-Manuel de Villena F, Kim WY, Magnuson T. Coexistent ARID1A-PIK3CA mutations promote ovarian clear-cell tumorigenesis through pro-tumorigenic inflammatory cytokine signalling. Nature communications. 2015; 6:6118.

Copp AJ. Death before birth: clues from gene knockouts and mutations. Trends Genet. 1995; 11:87–93. [PubMed: 7732578]

Coulibaly B, Sigaudy S, Girard N, Popovici C, Missirian C, Heckenroth H, Tasei AM, Fernandez C. Coffin-Siris syndrome with multiple congenital malformations and intrauterine death: towards a better delineation of the severe end of the spectrum. Eur J Med Genet. 2010; 53:318–321. [PubMed: 20624500]

Dallas PB, Pacchione S, Wilsker D, Bowrin V, Kobayashi R, Moran E. The human SWI-SNF complex protein p270 is an ARID family member with non-sequence-specific DNA binding activity. Molecular and cellular biology. 2000; 20:3137–3146. [PubMed: 10757798]

Danielian PS, Muccino D, Rowitch DH, Michael SK, McMahon AP. Modification of gene activity in mouse embryos in utero by a tamoxifen-inducible form of Cre recombinase. Curr Biol. 1998; 8:1323–1326. [PubMed: 9843687]

Deal KK, Cantrell VA, Chandler RL, Saunders TL, Mortlock DP, Southard-Smith EM. Distant regulatory elements in a Sox10-beta GEO BAC transgene are required for expression of Sox10 in the enteric nervous system and other neural crest-derived tissues. Developmental dynamics: an official publication of the American Association of Anatomists. 2006; 235:1413–1432. [PubMed: 16586440]

Ghislain J, Desmarquet-Trin-Dinh C, Gilardi-Hebenstreit P, Charnay P, Frain M. Neural crest patterning: autoregulatory and crest-specific elements co-operate for Krox20 transcriptional control. Development. 2003; 130:941–953. [PubMed: 12538520]

Griffin CT, Brennan J, Magnuson T. The chromatin-remodeling enzyme BRG1 plays an essential role in primitive erythropoiesis and vascular development. Development. 2008; 135:493–500. [PubMed: 18094026]

Inoue H, Furukawa T, Giannakopoulos S, Zhou S, King DS, Tanese N. Largest subunits of the human SWI/SNF chromatin-remodeling complex promote transcriptional activation by steroid hormone receptors. The Journal of biological chemistry. 2002; 277:41674–41685. [PubMed: 12200431]

Ishii M, Han J, Yen HY, Sucov HM, Chai Y, Maxson RE Jr. Combined deficiencies of Msx1 and Msx2 cause impaired patterning and survival of the cranial neural crest. Development. 2005; 132:4937–4950. [PubMed: 16221730]

Ishii M, Merrill AE, Chan YS, Gitelman I, Rice DP, Sucov HM, Maxson RE Jr. Msx2 and Twist cooperatively control the development of the neural crest-derived skeletogenic mesenchyme of the murine skull vault. Development. 2003; 130:6131–6142. [PubMed: 14597577]

Jacques-Fricke BT, Roffers-Agarwal J, Gammill LS. DNA methyltransferase 3b is dispensable for mouse neural crest development. PloS one. 2012; 7:e47794. [PubMed: 23094090]

Jiang X, Rowitch DH, Soriano P, McMahon AP, Sucov HM. Fate of the mammalian cardiac neural crest. Development. 2000; 127:1607–1616. [PubMed: 10725237]

Keyte A, Hutson MR. The neural crest in cardiac congenital anomalies. Differentiation. 2012; 84:25–40. [PubMed: 22595346]

Kirby ML, Hutson MR. Factors controlling cardiac neural crest cell migration. Cell adhesion & migration. 2010; 4:609–621. [PubMed: 20890117]

Kosho T, Okamoto N, Coffin-Siris Syndrome International, C. Genotype-phenotype correlation of Coffin-Siris syndrome caused by mutations in SMARCB1, SMARCA4, SMARCE1, and ARID1A. American journal of medical genetics. Part C, Seminars in medical genetics. 2014; 166C:262–275.

Kosho T, Okamoto N, Ohashi H, Tsurusaki Y, Imai Y, Hibi-Ko Y, Kawame H, Homma T, Tanabe S, Kato M, Hiraki Y, Yamagata T, Yano S, Sakazume S, Ishii T, Nagai T, Ohta T, Niikawa N, Mizuno S, Kaname T, Naritomi K, Narumi Y, Wakui K, Fukushima Y, Miyatake S, Mizuguchi T, Saitsu H, Miyake N, Matsumoto N. Clinical correlations of mutations affecting six components of the SWI/SNF complex: Detailed description of 21 patients and a review of the literature. Am J Med Genet A. 2013; 161:1221–1237. [PubMed: 23637025]

Kuratani SC, Kirby ML. Migration and distribution of circumpharyngeal crest cells in the chick embryo. Formation of the circumpharyngeal ridge and E/C8+ crest cells in the vertebrate head region. The Anatomical record. 1992; 234:263–280. [PubMed: 1384396]

Li L, Miano JM, Cserjesi P, Olson EN. SM22 alpha, a marker of adult smooth muscle, is expressed in multiple myogenic lineages during embryogenesis. Circulation research. 1996; 78:188–195. [PubMed: 8575061]

Li W, Xiong Y, Shang C, Twu KY, Hang CT, Yang J, Han P, Lin CY, Lin CJ, Tsai FC, Stankunas K, Meyer T, Bernstein D, Pan M, Chang CP. Brg1 governs distinct pathways to direct multiple aspects of mammalian neural crest cell development. Proc Natl Acad Sci U S A. 2013; 110:1738–1743. [PubMed: 23319608]

Lin CJ, Lin CY, Chen CH, Zhou B, Chang CP. Partitioning the heart: mechanisms of cardiac septation and valve development. Development. 2012; 139:3277–3299. [PubMed: 22912411]

Minoux M, Antonarakis GS, Kmita M, Duboule D, Rijli FM. Rostral and caudal pharyngeal arches share a common neural crest ground pattern. Development. 2009; 136:637–645. [PubMed: 19168678]

Nemani L, Barik R, Patnaik AN, Mishra RC, Rao AM, Kapur P. Coffin-Siris syndrome with the rarest constellation of congenital cardiac defects: A case report with review of literature. Annals of pediatric cardiology. 2014; 7:221–226. [PubMed: 25298701]

Nie Z, Xue Y, Yang D, Zhou S, Deroo BJ, Archer TK, Wang W. A specificity and targeting subunit of a human SWI/SNF family-related chromatin-remodeling complex. Molecular and cellular biology. 2000; 20:8879–8888. [PubMed: 11073988]

Nie Z, Yan Z, Chen EH, Sechi S, Ling C, Zhou S, Xue Y, Yang D, Murray D, Kanakubo E, Cleary ML, Wang W. Novel SWI/SNF chromatin-remodeling complexes contain a mixed-lineage leukemia chromosomal translocation partner. Molecular and cellular biology. 2003; 23:2942–2952. [PubMed: 12665591]

Nieto MA, Patel K, Wilkinson DG. In situ hybridization analysis of chick embryos in whole mount and tissue sections. Methods in cell biology. 1996; 51:219–235. [PubMed: 8722478]

Randall V, McCue K, Roberts C, Kyriakopoulou V, Beddow S, Barrett AN, Vitelli F, Prescott K, Shaw-Smith C, Devriendt K, Bosman E, Steffes G, Steel KP, Simrick S, Basson MA, Illingworth E, Scambler PJ. Great vessel development requires biallelic expression of Chd7 and Tbx1 in pharyngeal ectoderm in mice. J Clin Invest. 2009; 119:3301–3310. [PubMed: 19855134]

Santagati F, Rijli FM. Cranial neural crest and the building of the vertebrate head. Nat Rev Neurosci. 2003; 4:806–818. [PubMed: 14523380]

Santen GW, Aten E, Sun Y, Almomani R, Gilissen C, Nielsen M, Kant SG, Snoeck IN, Peeters EA, Hilhorst-Hofstee Y, Wessels MW, den Hollander NS, Ruivenkamp CA, van Ommen GJ, Breuning MH, den Dunnen JT, van Haeringen A, Kriek M. Mutations in SWI/SNF chromatin remodeling complex gene ARID1B cause Coffin-Siris syndrome. Nat Genet. 2012; 44:379–380. [PubMed: 22426309]

Santen GW, Aten E, Vulto-van Silfhout AT, Pottinger C, van Bon BW, van Minderhout IJ, Snowdowne R, van der Lans CA, Boogaard M, Linssen MM, Vijfhuizen L, van der Wielen MJ, Vollebregt MJ, Coffin-Siris C, Breuning MH, Kriek M, van Haeringen A, den Dunnen JT, Hoischen A, Clayton-Smith J, de Vries BB, Hennekam RC, van Belzen MJ. Coffin-Siris syndrome and the BAF complex: genotype-phenotype study in 63 patients. Human mutation. 2013; 34:1519–1528. [PubMed: 23929686]

Sausen M, Leary RJ, Jones S, Wu J, Reynolds CP, Liu X, Blackford A, Parmigiani G, Diaz LA Jr, Papadopoulos N, Vogelstein B, Kinzler KW, Velculescu VE, Hogarty MD. Integrated genomic analyses identify ARID1A and ARID1B alterations in the childhood cancer neuroblastoma. Nat Genet. 2013; 45:12–17. [PubMed: 23202128]

Schneider-Maunoury S, Topilko P, Seitandou T, Levi G, Cohen-Tannoudji M, Pournin S, Babinet C, Charnay P. Disruption of Krox-20 results in alteration of rhombomeres 3 and 5 in the developing hindbrain. Cell. 1993; 75:1199–1214. [PubMed: 7903221]

Schrier SA, Bodurtha JN, Burton B, Chudley AE, Chiong MA, D'Avanzo M G, Lynch SA, Musio A, Nyazov DM, Sanchez-Lara PA, Shalev SA, Deardorff MA. The Coffin-Siris syndrome: a proposed diagnostic approach and assessment of 15 overlapping cases. Am J Med Genet A. 2012; 158A:1865–1876. [PubMed: 22711679]

Soriano P. Generalized lacZ expression with the ROSA26 Cre reporter strain. Nat Genet. 1999; 21:70–71. [PubMed: 9916792]

Southard-Smith EM, Kos L, Pavan WJ. Sox10 mutation disrupts neural crest development in Dom Hirschsprung mouse model. Nat Genet. 1998; 18:60–64. [PubMed: 9425902]

Tsurusaki Y, Okamoto N, Ohashi H, Kosho T, Imai Y, Hibi-Ko Y, Kaname T, Naritomi K, Kawame H, Wakui K, Fukushima Y, Homma T, Kato M, Hiraki Y, Yamagata T, Yano S, Mizuno S, Sakazume S, Ishii T, Nagai T, Shiina M, Ogata K, Ohta T, Niikawa N, Miyatake S, Okada I, Mizuguchi T, Doi H, Saitsu H, Miyake N, Matsumoto N. Mutations affecting components of the SWI/SNF complex cause Coffin-Siris syndrome. Nat Genet. 2012; 44:376–378. [PubMed: 22426308]

Wilkinson DG, Bhatt S, Chavrier P, Bravo R, Charnay P. Segment-specific expression of a zinc-finger gene in the developing nervous system of the mouse. Nature. 1989; 337:461–464. [PubMed: 2915691]

Wilkinson DG, Nieto MA. Detection of messenger RNA by in situ hybridization to tissue sections and whole mounts. Methods in enzymology. 1993; 225:361–373. [PubMed: 8231863]

Zerucha T, Stuhmer T, Hatch G, Park BK, Long Q, Yu G, Gambarotta A, Schultz JR, Rubenstein JL, Ekker M. A highly conserved enhancer in the Dlx5/Dlx6 intergenic region is the site of cross-regulatory interactions between Dlx genes in the embryonic forebrain. The Journal of neuroscience: the official journal of the Society for Neuroscience. 2000; 20:709–721. [PubMed: 10632600]

Zucker RM, Hunter ES 3rd, Rogers JM. Apoptosis and morphology in mouse embryos by confocal laser scanning microscopy. Methods. 1999; 18:473–480. [PubMed: 10491277]

- SWI/SNF BAF-A chromatin remodeling complex is essential for neural crest development
- Loss of BAF-A affects the circumpharygeal cardiac neural crest
- Biochemically distinct SWI/SNF complexes regulate separable events in neural crest development

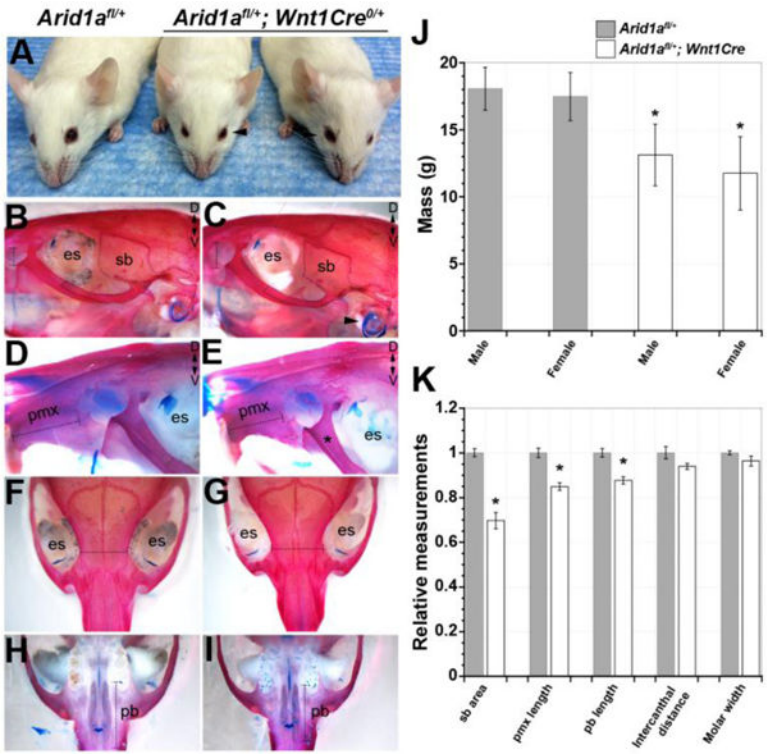

Figure 1. Heterozygous *Arid1a*$^{fl/+}$*; Wnt1Cre* mice display mild craniofacial defects

(A) Images depict 8 week-old mice *Arid1a*$^{fl/+}$ littermate control and *Arid1a*$^{fl/+}$*; Wnt1Cre*. Arrowheads in *A* denote sunken eyes. (B–I) Alizarin red and alcian blue stained skull preparations of 8 week-old *Arid1a*$^{fl/+}$ littermate control and *Arid1a*$^{fl/+}$*; Wnt1Cre* mice. Arrowhead in *C* denotes the ear canal. Asterisk in *E* denotes the jugal bone. (J) Graph of body mass measurements of 8–10 week-old male and female *Arid1a*$^{fl/+}$ littermate control and *Arid1a*$^{fl/+}$*; Wnt1Cre* mice. (K) Graph of morphometric measurements of *Arid1a*$^{fl/+}$*; Wnt1Cre* skull bones, as compared to littermate controls. Significant differences based on the average measurement ±standard deviation were calculated using a two-tailed Student's *t* test (*p-value < 0.05). es, eye socket; sb, squamosal bone; pmx, pre-maxilla bone; pb, palatine bone.

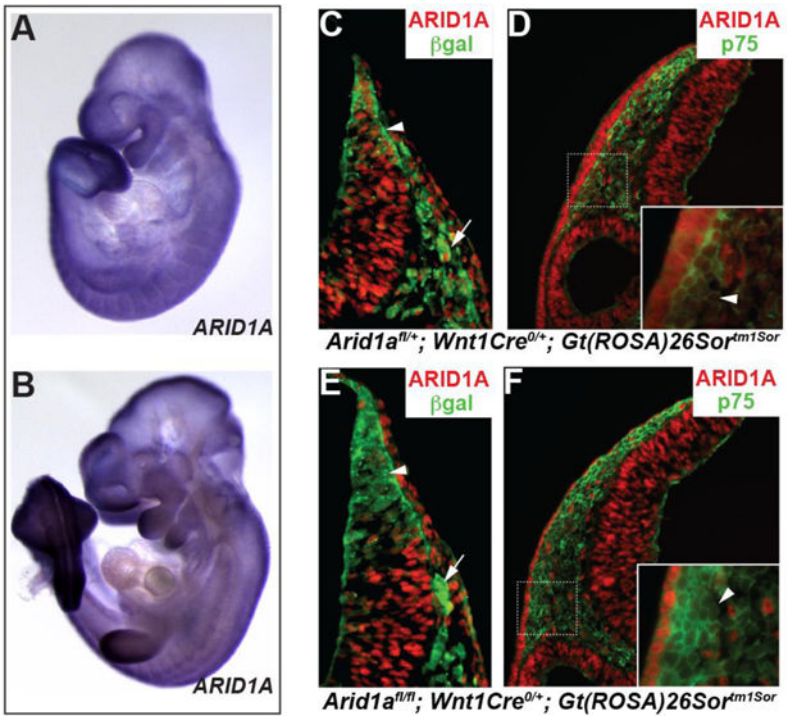

Figure 2. ARID1A is inactivated in NCCs expressing the *Wnt1CRE* transgene

(A,B) Whole mount images of E9.5 (A) and E10.5 (B) embryos hybridized with antisense ARID1A probes. (C–F) ARID1A and β-GALACTOSIDASE (β-GAL) or P75 fluorescent immunostaining of E10.5 *Arid1a*$^{fl/fl}$*; Gt(ROSA)26*^{tm1Sor}*; Wnt1Cre* and *Arid1a*$^{fl/+}$*; Gt(ROSA)26*^{tm1Sor}*; Wnt1Cre* dorsal neural tube sections. High magnification images of *B* and *D* are shown inset. Arrowheads in *A* and *C* denote cells in the dorsal neural tube or neural fold region. Arrows in *A* and *C* denote migrating β-GAL-positive NCCs. Arrowheads in *B* and *D* denote P75-positive NCCs in the head mesenchyme.

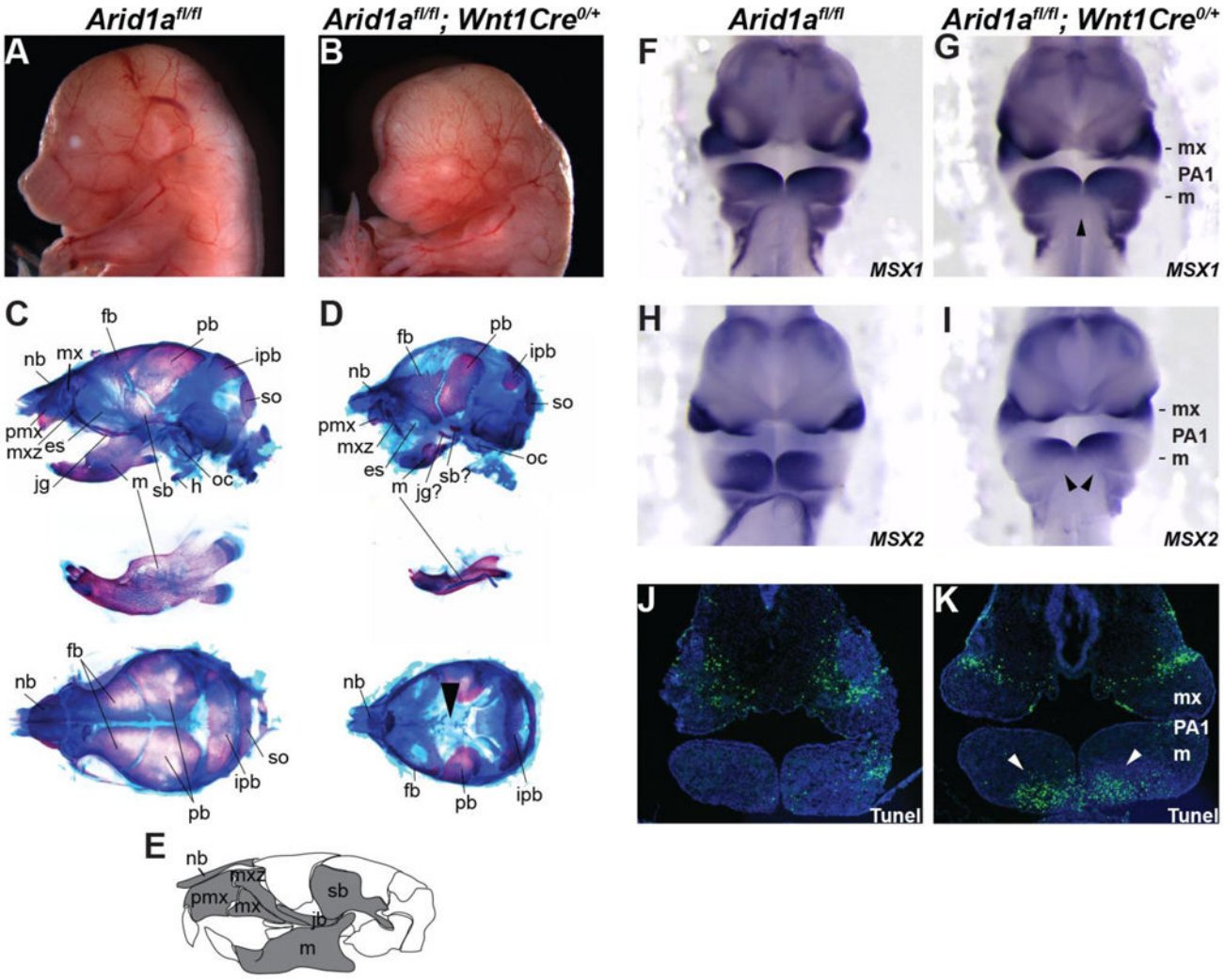

Figure 3. Homozygous loss of ARID1A in NCCs leads to severe craniofacial defects

(A,B) Whole mount images of head and upper trunk E16.5 *Arid1a*$^{fl/fl}$ and *Arid1a*$^{fl/fl}$*; Wnt1Cre* embryos. (C,D) Whole mount images of alizarin red and alcian blue-stained skull preparations of E17.5–18.0 *Arid1a*$^{fl/fl}$ and *Arid1a*$^{fl/fl}$*; Wnt1Cre* mice. Arrowhead in *D* denotes an open head foramen. (E) Cartoon depiction of cranial bones affected in *Arid1a*$^{fl/+}$*; Wnt1Cre* and *Arid1a*$^{fl/fl}$*; Wnt1Cre* mice. (F–I) Whole mount, frontal images of E10.5 *Arid1a*$^{fl/fl}$ and *Arid1a*$^{fl/fl}$*; Wnt1Cre* embryonic heads hybridized with MSX1 and MSX2 antisense probes and oriented to depict the MSX1/2 positive mesenchyme of the cranial pharyngeal arches (PA). Arrowheads in *G* and *I* depict the ventral boundary of MSX1 and MSX2 expression in PA1 and the dorsal boundary of the pharyngeal pouch. (J,K) TUNEL images of frontal sections through PA1 of E10.5 *Arid1a*$^{fl/fl}$ and *Arid1a*$^{fl/fl}$*; Wnt1Cre* embryonic heads. Arrowheads in *K* depict TUNEL-positive cells in the ventral half of the mandibular portion of PA1. nb, nasal bone; mx, maxilla; fb, frontal bone; pb, parietal bone; ipb, interparietal bone; so, supraoccipital bone; oc, otic canal; h, hyoid; sb, squamosal bone; m, mandible; jg, jugal bone; es, eye socket; mxz, maxilla zygomatic process; pmx, premaxilla.

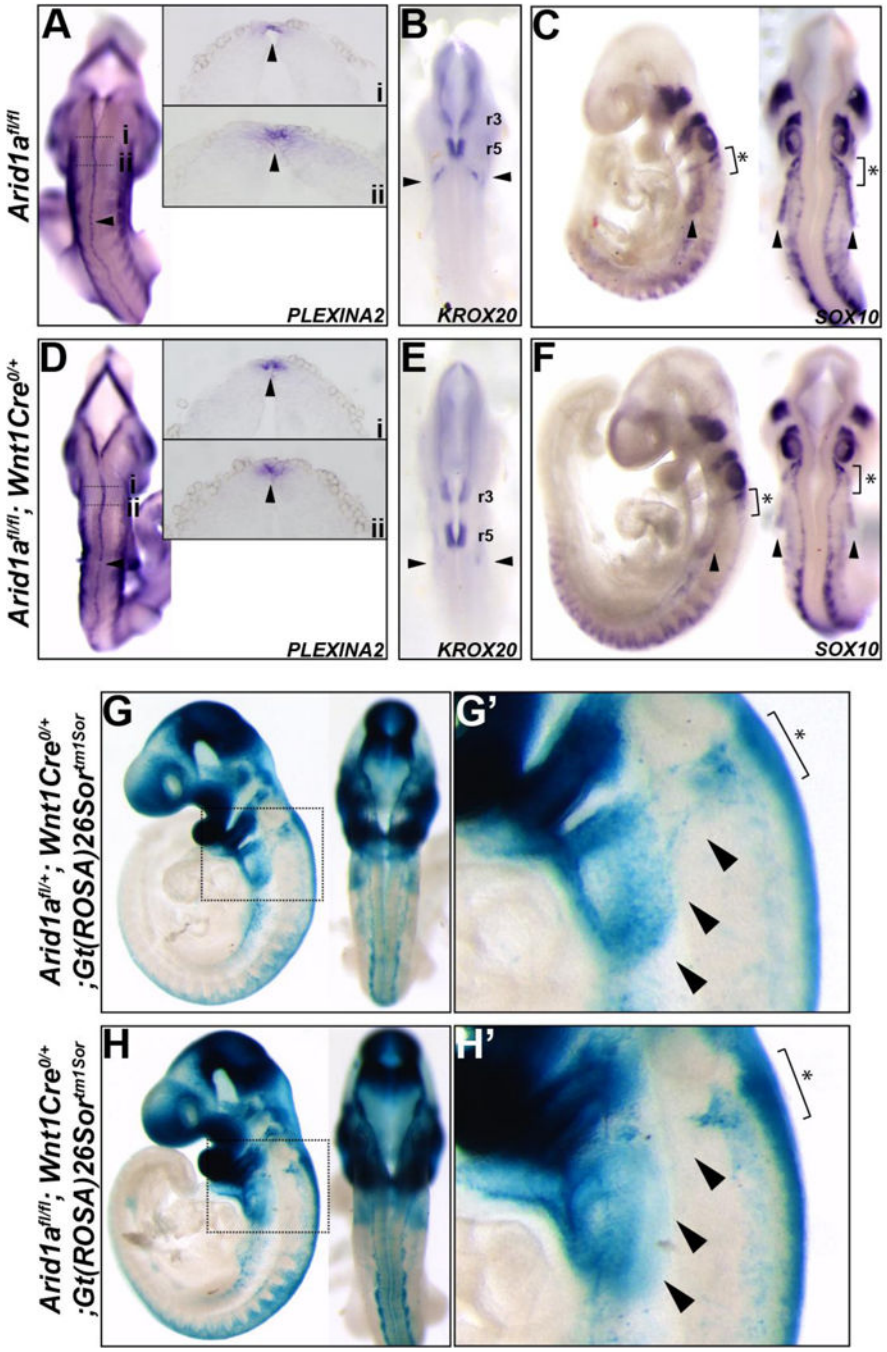

Figure 4. ARID1A loss in NCCs affects early cardiac NCC migration

(A,D) Whole mount images of E9.5 *Arid1a*$^{fl/fl}$ and *Arid1a*$^{fl/fl}$*; Wnt1Cre* embryos hybridized with PLEXINA2 antisense probes. Cross-sectional images of dorsal neural tube regions demarcated by dotted lines are shown inset. Arrowheads in *A* and *E* denote PLEXINA2-positive premigratory NCCs in the dorsal neural. (B,E) Whole mount images of E9.5 *Arid1a*$^{fl/fl}$ and *Arid1a*$^{fl/fl}$*; Wnt1Cre* embryos hybridized with KROX20 antisense probes. Arrowheads in *B* and *E* denote KROX20-positive post-otic migratory cardiac NCC streams. (C,F) Whole mount images of E9.5 *Arid1a*$^{fl/fl}$ and *Arid1a*$^{fl/fl}$*; Wnt1Cre* embryos hybridized

with SOX10 antisense probes. Arrowheads in *C* and *F* denote SOX10-postive NCCs within the circumpharyngeal ridge. (G,H) Whole mount images of lacZ-stained 9.5 *Arid1a*$^{fl/+}$*; Gt(ROSA)26*^{tm1Sor}*; Wnt1Cre* and *Arid1a*$^{fl/fl}$*; Gt(ROSA)26*^{tm1Sor}*; Wnt1Cre* embryos. High magnification images of regions demarcated by dotted lines in G and H are shown in G′ and H'. Arrowheads in G′ and *H′* denote β-GAL-positive NCCs within the circumpharyngeal ridge. Asterisk in *C, F, G′, and H'* denote early migrating post-otic and circumpharyngeal cardiac neural crest cells. r3, rhombomere 3; r5, rhombomere 5.

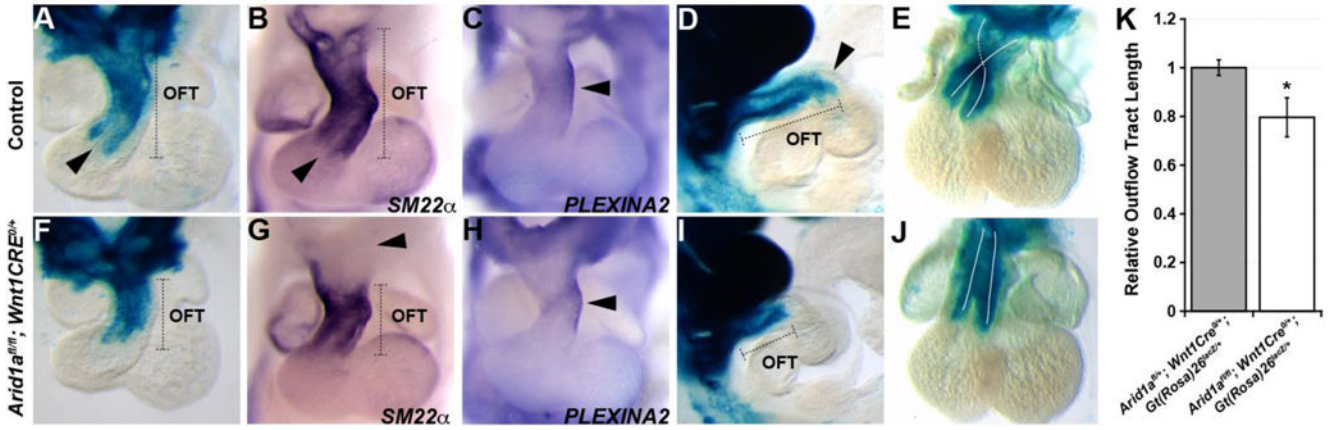

Figure 5. Outflow tract length and conotruncal septation are affected by ARID1A loss in cardiac NCCs

(A,B,C and F,G,H) Frontal-view images of lacZ-, SM22α, or PLEXINA2-stained E10.5 *Arid1a*$^{fl/fl}$*; Gt(ROSA)26*^{tm1Sor}*; Wnt1Cre* and control hearts. Arrowheads in *A* and *B* denote the early aorticopulmonary septum. Arrowheads in *C* and *H* denote PLEXINA2 expression domain in OFT. Arrowhead in *G* denotes the aortic sac. (D,I) Sagittal-view images of lacZ-stained E10.5 *Arid1a*$^{fl/fl}$*; Gt(ROSA)26*^{tm1Sor}*; Wnt1Cre* and control outflow tracts. Arrowhead in *D* denotes the early separation of future pulmonary artery and aorta. (E,J) Frontal-view images of lacZ-stained E11.5 *Arid1a*$^{fl/fl}$*; Gt(ROSA)26*^{tm1Sor}*; Wnt1Cre* and control hearts. (K) Graph of relative outflow tract length measurements for lacZ-stained 10.5 *Arid1a*$^{fl/+}$*; Gt(Rosa)26*$^{lacZ/+}$*; Wnt1Cre* and *Arid1a*$^{fl/fl}$*; Gt(Rosa)26*$^{lacZ/+}$*; Wnt1Cre* embryos. Significant differences based on the average measurement ±standard deviation were calculated using a two-tailed Student's *t* test (*p-value < 0.05). OFT, outflow tract.

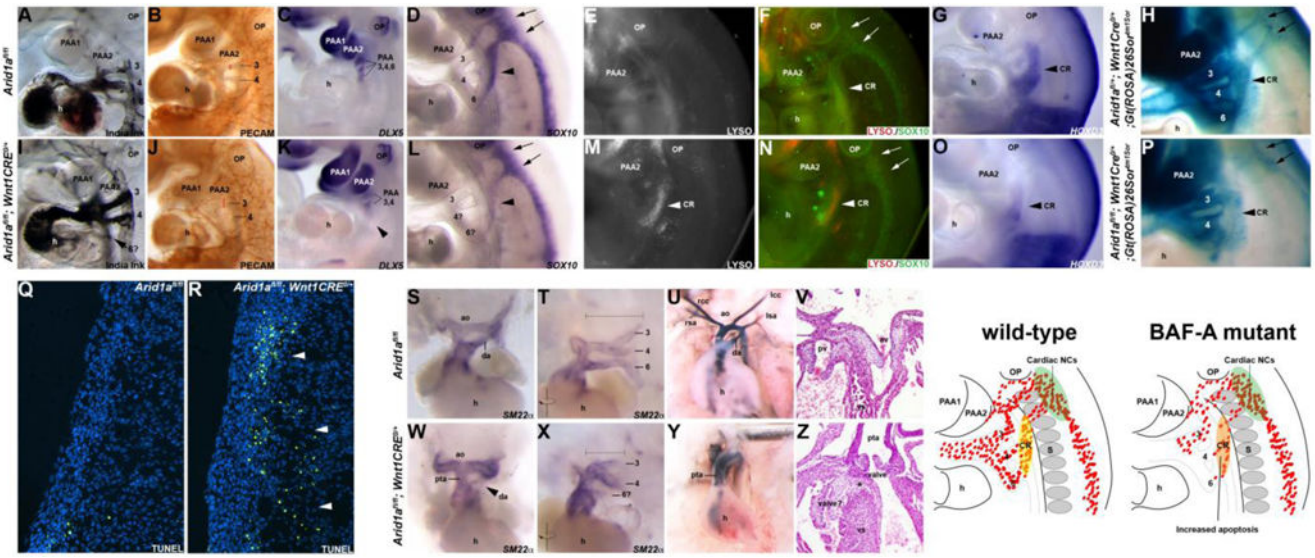

Figure 6. BAF-A complexes are required for cardiac circumpharyngeal NCC migration and the formation of the ductus arteriosus

Whole mount, sagittal-view images of E10.5 *Arid1a*$^{fl/fl}$ and *Arid1a*$^{fl/fl}$*; Wnt1Cre* embryos injected with India ink in *A* and *I*, stained with anti-PECAM antibodies in *B* and *J*, hybridized with DLX5, SOX10, or HOXD3 antisense probes, or co-stained with anti-SOX10 antibodiesand Lysotracker Red in E, *F*, *M*, and *N*. Arrow in *I* denotes a non- patent PAA6 artery. Arrowhead in *K* shows undetectable DLX5 expression in PAA6. Arrowhead in *D* and L denotes the SOX10-positive, migratory circumpharyngeal cardiac NCC stream. Arrows in *D*, *L*, F and *N* denote the SOX10-positive post-otic and rhombomeres 5–8 cardiac NCC streams. Arrowheads *in* M *and N* denote Lysotracker Red-positive cells in the circumpharyngeal ridge. (H,P) Sagittal images of lacZ-stained 10.5 *Arid1a*$^{fl/+}$*; Gt(Rosa)26*$^{lacZ/+}$*; Wnt1Cre* and *Arid1a*$^{fl/fl}$*; Gt(Rosa)26*$^{lacZ/+}$*; Wnt1Cre* embryos. Arrows in *H* and *P* denote β-GAL positive post-otic and rhombomeres 5–8 cardiac NCC streams. (Q,R) TUNEL images of frontal sections the circumpharygeal ridge of E10.5 *Arid1a*$^{fl/fl}$ and *Arid1a*$^{fl/fl}$*; Wnt1Cre* embryos. (S, T, W, X) Whole mount images of E12.5 *Arid1a*$^{fl/fl}$ and *Arid1a*$^{fl/fl}$*; Wnt1Cre* embryonic hearts hybridized with SM22α-antisense probes. The images shown in *T* and *X* depict SM22α-stained hearts that have been rotated to better visualize the PAAs. Arrowhead in *W* denotes a non-patent ductus arteriosus. (U,Y) India ink injected E16.5 *Arid1a*$^{fl/fl}$ and *Arid1a*$^{fl/fl}$*; Wnt1Cre* hearts. (V,Z) Hematoxylin and Eosin stained histological sections of E16.5 *Arid1a*$^{fl/fl}$ and *Arid1a*$^{fl/fl}$*; Wnt1Cre* hearts. Asterisk in *Z* denotes a ventricular septal defect. h, heart; paa, pharyngeal arch artery; cr, circumpharyngeal ridge; ao, aorta; da, ductus arteriosus; rcc, right common carotid; rsa, right subclavian artery; lcc, left common carotid; lsa, left subclavian artery; pta, patent truncus arteriosus; pv, pulmonary valve; av, aortic valve; vs, ventricular septum.

Table 1

Arid1a$^{fl/fl}$*; Wnt1Cre* embryos die *in utero*

Age	Total	Expected	Observed
E9.0–12.5	130	33	37
E13.0–14.5	63	16	16
E15.0–P0	46	12	5
Weaning	44	11	0

Table 2

Summary of India ink injections

		Arid1a$^{fl/fl}$	*Wnt1CRE$^{0/+}$; Arid1a$^{fl/+}$*	*Wnt1CRE$^{0/+}$; Arid1a$^{fl/fl}$*
E10.5 Total # of embryos:		11	9	12
Normal:		10	7	0
	Abnormal:			
Left 3rd PAA	Thin Patent	–	–	4 (33%)
	Non-Patent	–	–	–
Left 4th PAA	Thin Patent	–	–	5 (42%)
	Non-Patent	1 (9%)	–	2 (17%)
Left 6th PAA	Thin Patent	–	1 (11%)	3 (25%)
	Non-Patent	1 (9%)	1 (11%)	9 (75%)
Right 3rd PAA	Thin Patent	–	–	4 (33%)
	Non-Patent	–	–	–
Right 4th PAA	Thin Patent	–	–	4 (33%)
	Non-Patent	–	–	3 (25%)
Right 6th PAA	Thin Patent	–	–	3 (25%)
	Non-Patent	1 (9%)	1 (11%)	9 (75%)